JOURNAL OF GEOPHYSICAL RESEARCH, VOL. 113, B05406, doi:10.1029/2007JB005334, 2008

Feeding system and magma storage beneath Mt. Etna as revealed by recent inflation/deflation cycles

Alessandro Bonforte,[1] Alessandro Bonaccorso,[1] Francesco Guglielmino,[1] Mimmo Palano,[1] and Giuseppe Puglisi[1]

Received 17 August 2007; revised 29 December 2007; accepted 21 January 2008; published 16 May 2008.

[1] Ground deformation at Mt. Etna detected by three GPS surveys carried out in 2004, 2005, and 2006 is analyzed. The data set encompasses the 2004–2005 eruptions and foreruns those of 2006. A wide deflation of the entire volcano was detected from 2004 to 2005, accompanying the 2004–2005 eruption; conversely an evident inflation phase, from 2005 to 2006, followed this eruption and preceded the 2006 one. In both cases, the deflation-inflation cycle was accompanied by a continuous seaward motion of the eastern flank. We inverted both data sets (2004–2005 deflation and 2005–2006 inflation) using an optimization algorithm based on the Genetic Algorithm (GA) in order to detect the ground deformation sources. The wide contraction measured during the eruption reveals the drainage of a sill-shaped magma reservoir located by data inversions at a depth of about 4.5 km b.s.l. The pressurizing source modeled for the 2005–2006 time interval indicates a refilling of the shallower near-vertical plumbing system of the volcano. This could indicate a change in the geometry of the feeding system, active after the 2004–2005 eruption, with a new and shallower magma storage that could have enabled the resumption of volcanic activity that was observed at summit craters in 2006. These results improve the imaging of the plumbing system of Mt. Etna volcano.

Citation: Bonforte, A., A. Bonaccorso, F. Guglielmino, M. Palano, and G. Puglisi (2008), Feeding system and magma storage beneath Mt. Etna as revealed by recent inflation/deflation cycles, *J. Geophys. Res.*, *113*, B05406, doi:10.1029/2007JB005334.

1. Introduction

[2] At Mount Etna, a dense GPS network (Figure 1) is measured periodically (once a year, at least) and consists of about seventy benchmarks. The time series of ground motion measurements made using this network began in 1988; from then on, its configuration has been improved so that it now covers the entire volcanic area [*Bonforte and Puglisi*, 2003], with particular emphasis on the eastern flank [*Puglisi et al.*, 2004]. After the 1991–1993 lateral eruption, accompanied by a significant contraction of the measured network, a continuous and fairly constant inflation phase started as shown by the cumulative areal dilatation of the network (Figure 2a). This inflation phase culminated with the 2001 and 2002–2003 lateral eruptions.

[3] After these eruptions, in the period 2003–2006, the volcano showed two interesting phenomena: (1) a renewal of an overall inflation marked by two further eruptions (2004–2005 and 2006) during which the volcano showed a deflation and (2) a constant and marked eastward sliding of the eastern flank of the volcano.

[4] The 2004–2005 eruption was a passive eruption induced by the exceptional sliding rate of the eastern flank of the volcano [*Bonaccorso et al.*, 2006]. The magma outpouring provoked a general deflation of the volcano, as was well testified by the contraction of the GPS network. After the end of the 2004–2005 eruption, the GPS network recorded a renewal of the inflation that led to the 2006 eruption. Besides the deflation-inflation sequence, the eastern flank of the volcano showed an absolutely independent dynamics, being affected by a fairly constant seaward motion [see *Bonforte and Puglisi*, 2003, 2006; *Puglisi and Bonforte*, 2004; *Bonaccorso et al.*, 2006; *Palano et al.*, 2007]. In fact, all stations lying on this side of the volcano show similar displacements during the 2004–2005 and 2005–2006 intervals. Here, we present original data from the July 2004–June 2006 time interval, encompassing the 2004–2005 lateral eruption (deflation phase) and preceding the July–December 2006 eruption (inflation phase). We inverted and modeled the ground deformation pattern of these two phases in order to infer the storage sources and improve the imaging of the plumbing system of Etna.

2. Structural Setting

[5] Mt. Etna volcano is located within a complex regional tectonic setting in northern Sicily involving a compressive N–S stress regime and an E–W extensional regime, observable along the eastern coast of Sicily (see *Bousquet and Lanzafame* [2004] for an overall review). In addition, the eastern flank of the volcano shows an eastward, shallow, sliding movement, probably due to the interrelationship between gravity instability and magma intrusion [e.g.,

[1] Istituto Nazionale di Geofisica e Vulcanologia, Catania, Italy.

0148-0227/08/2007JB005334$09.00

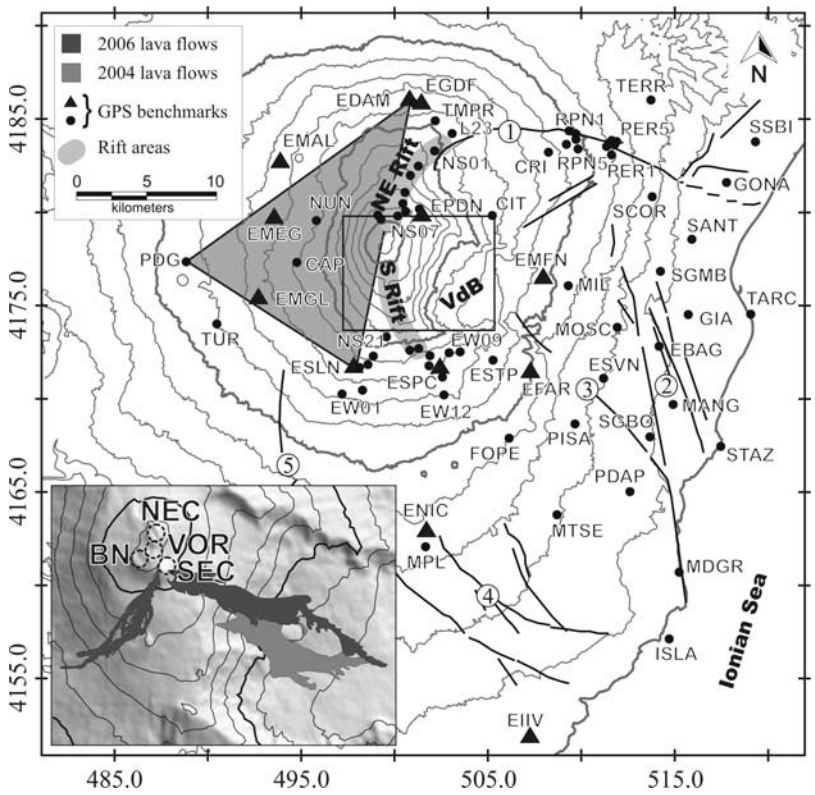

Figure 1. Sketch map of Mt. Etna with main active faults and GPS network. 1: Pernicana fault; 2: "Timpe" fault system; 3: Santa Venerina fault; 4: Mascalucia-Tremestieri-Trecastagni fault system; 5: Ragalna fault. Triangles and circles indicate permanent and periodically measured GPS stations, respectively. The area of the summit craters is detailed in the inset, where the lava flows are also reported; BN = Bocca Nuova, NEC = Northeast crater, VOR = Voragine, SEC= Southeast crater. The shadowed triangle was used for computation of the areal dilatation of the western part of Mt. Etna. VdB, Valle del Bove. Coordinates in UTM projection, zone 33N.

Borgia et al., 1992; *Lo Giudice and Rasà*, 1992; *Rust and Neri*, 1996; *Bonforte and Puglisi*, 2003, 2006; *Rust et al.*, 2005]. The Pernicana fault system (Figure 1) represents the northern boundary of this unstable sector. Westward, this fault joins the NE Rift, representing one of the most active volcanic features (Figure 1). The southern part of the western boundary of the sector is demarcated by the S Rift [*Rasà et al.*, 1996] joining, south-eastward, the Mascalucia-Tremestieri-Trecastagni fault system (Figure 1). This sector of the volcano shows a greater complexity of flank motion, as revealed also by InSAR data [*Borgia et al.*, 2000; *Froger et al.*, 2001; *Lundgren et al.*, 2004]. This fault system is made up of a number of NNW-SSE-striking faults showing evident right lateral displacement and is also characterized by very shallow seismicity, with focal depths typically of 1–2 km. It has been interpreted as the southern boundary of the sliding sector [*Rasà et al.*, 1996].

3. Recent Eruptive Activity

3.1. The 2004–2005 Eruption

[6] After the 2002–2003 eruption, the volcano continued to inflate and the eastern flank accelerated its downward movement toward the East [*Bonaccorso et al.*, 2006]. On 7 September 2004, volcanic activity resumed on Mt. Etna (Figure 2b) by the opening of an effusive vent at the base of the SE summit crater (SEC) at about 3000 m above sea level (a.s.l.). In the following two days, the eruptive fissure propagated downward toward the Valle del Bove (VdB) depression and the lava poured out inside this valley. The eruption lasted until 12 March 2005 and, after three months of eruption, lava volumes were estimated between 18.5 and 32×10^6 m^3 [*Burton et al.*, 2005]. This eruption onset was completely "silent" [*Bonaccorso et al.*, 2006] in the sense that there was no volcanic activity at the summit craters, no significant gas emission, no seismic tremor or seismicity (Figure 2c), no ground deformation which are usually observed during intrusion processes. *Bonaccorso et al.* [2006] suggested that this peculiar eruption was caused by the exceptional tension, created on the uppermost part of the volcano by the high-rate of sliding of the eastern flank of the volcano, which favored the opening of the fracture feeding the magma drainage. Later on, the ground deformation revealed a clear deflation during the course of the eruption (Figures 2a and 3), which will be analyzed in section 5.1.

3.2. The Eruptive Activity in 2006

[7] After the 2004 eruption, the ground deformation recorded the onset of an inflation phase (Figures 2a and 4). Volcanic activity re-started at summit craters of Mt. Etna during the night of 14 July 2006, when a fissure opened on the eastern flank of the SEC, with the same azimuth of the

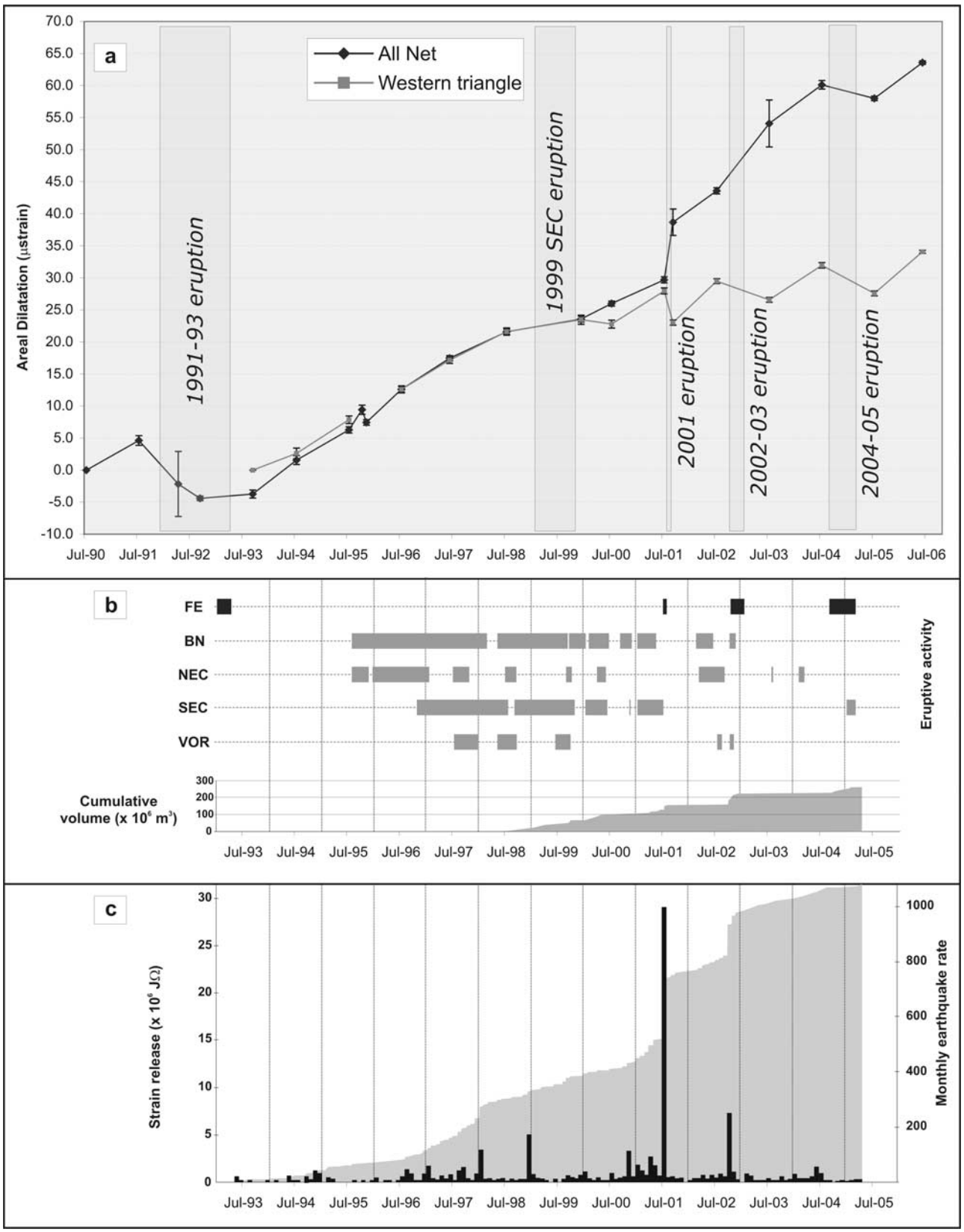

Figure 2. (a) Cumulative areal dilatation since 1990, computed both for the entire GPS network and for the EDAM-PDG-ESLN triangle (see Figure 1). (b) (redrawn from *Allard et al.* [2006]): Eruptive activity at summit craters and flank eruptions (FE). Lower portion of frame b shows cumulative eruptive volume (expressed as dense rock equivalent). (c) (redrawn from *Allard et al.* [2006]): Monthly number of earthquakes (vertical bars) and cumulative strain release (shaded area).

2004 eruption. Three vents opened along the fissure field at about 3000 m a.s.l., two of them emitting two lava flows (joining into one after a few hundred meters) propagating eastward inside the VdB. Like the 2004 eruption, this eruption onset was not accompanied by evident geophysical parameter changes (seismicity and ground deformation related to dyke intrusion and fissure opening), even if the 2006 eruption was characterized by strong degassing from the uppermost vent, with strong Strombolian activity and, consequently, an increased tremor during the entire duration of the eruptive activity. This eruption lasted a little more than one week, ending on 23 July 2006. The volcanic activity restarted at SEC at the end of August 2006, with Strombolian activity and the formation of new short lava flows expanding eastward for about 1 km; activity that lasted until mid September. A new eruptive fracture opened on 13 October from the East base of the SEC, trending ESE-WNW and reaching an altitude of 2800 m a.s.l.; here, effusive activity started forming lava flows spreading eastward. Also this fracture opened with no geophysical parameter changes, as a new fracture field formed on 26 October on the opposite side of the SEC, involving also the southern flank of the Bocca Nuova (BN) crater at 3050 m of altitude. Only episodic increases in volcanic tremor accompanied the periods characterized by more intense degassing and Strombolian activity at SEC. The eruption activity ended on 15 December 2006.

4. GPS Data

[8] GPS surveys are carried out in static mode, with measurement sessions lasting from four to twenty-four hours (especially for the reference stations), and in semi-kinematic mode (stop-and-go) along two profiles crossing the upper part of the volcano in N–S and E–W directions [*Puglisi and Bonforte*, 2004; *Bonforte et al.*, 2004]. All benchmarks along these profiles are self-centering (as most of the static network), to improve the measurement accuracy, and are measured twice, forward and backward, with 3-minute occupations. In 2005, the reference frame of the Mt. Etna network was improved by the installation of new stations (CTNV, MONT, ECES) that allow 24-h sessions to be carried out during the entire duration of the survey. So, during the 2005 survey, both old and new reference stations were measured; in 2006, only the new reference stations were measured.

[9] The data collected during the surveys, combined with those coming from permanent stations, were processed in order to obtain the vector components for each baseline. The data were processed using the L3 phase combination, for baselines longer than 10 km, in order to eliminate the ionospheric effect, and always using NGS (National Geodetic Survey) antenna calibration models and precise ephemeredes computed by the IGS (International Geodetic Service), adopting the usual procedure for the Etna network [*Puglisi et al.*, 2001; *Bonforte and Puglisi*, 2003].

[10] A free adjustment is performed after having processed all (static and kinematic) GPS data. Finally, the network is then fixed assuming an appropriate set of coordinates for the reference frame. The 2004 and 2005 surveys were fixed to the same reference frame, through the EIIV, CES and ROC coordinates. A second adjustment process was performed for the 2005 survey in order to obtain a precise set of coordinates for the new reference stations in the ITRF2000 frame, including NOT1, MATE, CAGL and LAMP IGS stations and fixing their positions at the epoch 2005.6, calculated by using the IGS station velocities. Then, the 2006 survey solution is referred to the same frame of the 2005 survey, by fixing the coordinates of MONT, ECES and EIIV resulting from the 2005 second adjustment. Final results of the processing are the station coordinates, with associated errors (2-sigma) of the order of 3–4 mm for the horizontal components and 6–7 mm for the vertical one, for all three surveys. A complete list of the measured displacements for the 2004–2005 and 2005–2006 periods is provided in Tables 1 and 2, respectively.

5. Ground Deformation Pattern

[11] The overall ground deformation pattern is well summarized by the areal dilatation of the network (Figure 2a). This is a parameter of the strain tensor, computed by using a least squares algorithm based on the approach suggested by *Livieratos* [1980], which takes into account the strain calculated for all ellipsoid distances between GPS stations. In order to guarantee homogeneity in the strain tensor computation over time and to exclude the bias due to the volcano sliding dynamics, the areal dilatation is calculated excluding most of the benchmarks lying on the eastern flank. In particular, we excluded the stations initially belonging to the "Ionica" network, [see *Bonforte and Puglisi*, 2006] that were included in the Mt. Etna GPS surveys since 2001.

[12] A constant inflation phase is evident after the 1991–1993 lateral eruption. This inflation shows a fairly constant rate until the beginning of the activity leading to the violent lateral 2001 and 2002–2003 eruptions. The 2002–2003 eruption, characterized by two intrusions along the S and NE Rifts (Figure 1), provoked an acceleration of areal dilatation. The main contribution to this came from the 2002 NE dike, which induced bigger displacements and also pushed the eastern flank, accelerating its sliding [*Bonaccorso et al.*, 2006; *Bonforte et al.*, 2007b]. The first evident contraction episode, involving the entire GPS network, occurred only after the 2004–2005 eruption (Figure 2a).

[13] In order to separately investigate the deformation of the stable part of the volcano, unaffected by the sliding dynamics, the areal dilatation was computed also for the EDAM-PDG-ESLN triangle (see Figure 1 for benchmarks position) covering the central-western area of the volcano. The areal dilatation of this triangle well matches the trend of the entire network until 1999, evidencing how the volcano was affected by a uniform deformation (Figure 2a). Conversely, Figure 2a illustrates the different behavior of the western side of the volcano since the beginning of the new eruptive phase marked by the 2001 eruption. In particular, the trend of the dilatation of the western flank clearly shows contraction due to the phase related to the deflation due to the 2001 lava effusion and pressure discharge, while the dilatation of the whole network is greatly affected by the flank instability triggered by the intrusions that force the volcano to spread laterally toward the east and south amplifying the overall dilatation.

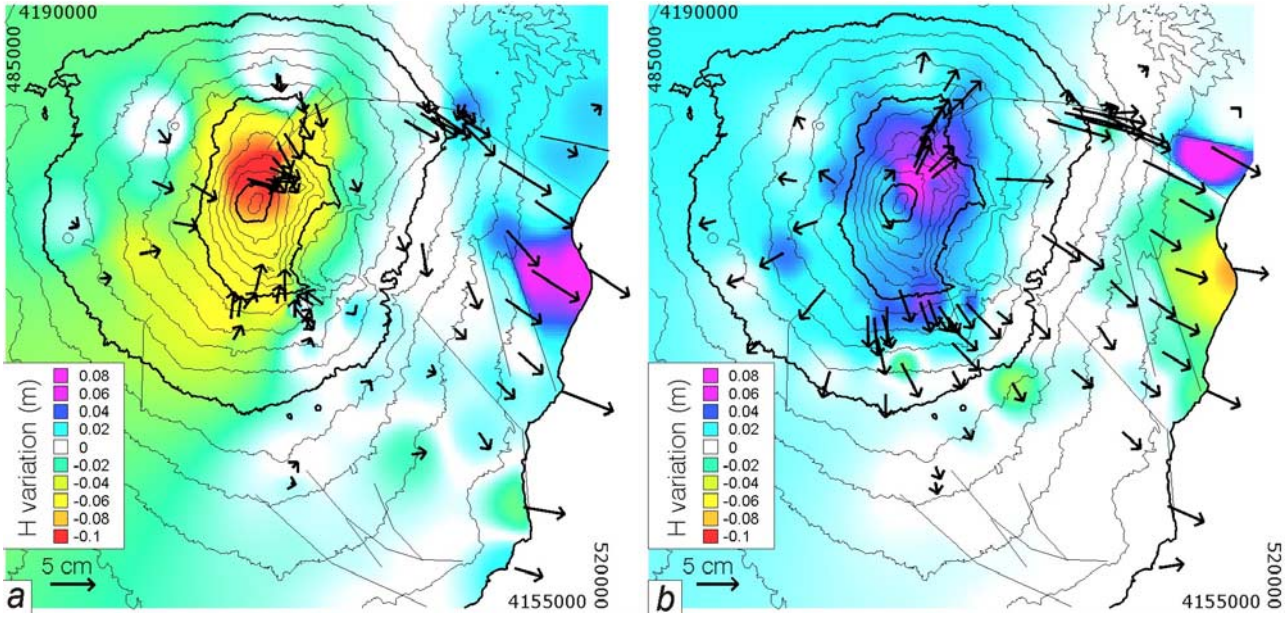

Figure 3. Displacement vectors and height variations from the comparison between (a) July 2004–July 2005 and (b) July 2005–June 2006. The arrows represent the horizontal displacement vectors, while the vertical displacement is presented by a color map obtained by interpolating the measurements relevant to each benchmark. The values are gridded by taking into account the main known faults as discontinuities in the interpolation. The error ellipses of the displacements calculated at the confidence interval of 95% are in the order of a few millimeters, and for this reason they are not shown in the figures.

5.1. 2004–2005 Deflating Phase

[14] By comparing the coordinates resulting from 2004 and 2005 surveys, we can analyze the ground deformation accompanying the entire 2004–2005 eruption; 3D displacements were obtained and are shown in Figure 3a. While the horizontal displacements are reported by vectors at each station, the vertical motions measured at each station are interpolated across the area, but constrained by the known main faults, as discontinuities in the gridding process. The resulting pattern reveals a volcano-wide deflation. A marked radial (centripetal) pattern of the displacement vectors is evident from Figure 3a on the western, southern and northern flanks of the volcano, where horizontal displacements of about 3 cm are detected, decreasing from higher to lower altitude. This radial pattern is disturbed only on the NE Rift, where the GPS stations show a general southeastward motion, as does the entire eastern flank of the volcano. All this sector of Mt. Etna, as previously detected from GPS data by *Bonforte and Puglisi* [2003], shows an independent behavior, with an overall seaward motion. The abrupt decay of the displacements on the northern part along the Pernicana fault confirms the key role played by this structure in decoupling the sliding sector from the stable part of the volcano. The magnitude of the horizontal displacements apparently decreases from more than 6 cm along the coastline to almost zero on the upper part of the eastern flank and this gradient could be due to the stronger effect of the contraction in the central part of the volcano that on this flank acts in the opposite direction to that of the sliding. The different motion affecting the stations lying on different sides of the main faults on the eastern flank confirms the segmentation of this sector of the volcano into several blocks, as inferred by *Walter et al.* [2005] from geological data, showing different deformation styles and velocities, and confirming the patterns detected by *Bonforte and Puglisi* [2006] from geodetic data. In synthesis, the period astride the 2004–2005 event shows a contraction associated with the eruption and a continuous and independent sliding movement of the eastern sector.

5.2. 2005–2006 Inflating Phase

[15] By comparing the 2005 and 2006 GPS surveys (Figure 3b), the ground deformation following the 2004–2005 eruption and preceding the resumption of activity in 2006 can be studied. It is evident that this is a recharging phase where the volcano began to inflate, showing an opposite ground deformation pattern to that detected for the previous year. In fact, a radial (centrifugal) pattern of the horizontal displacements from a center located very close to the summit craters, on their northern sector, is clearly visible. The height variations show a general uplift of the edifice, with a maximum of about 8 cm on the uppermost northeastern flank. Conversely, the eastern flank continues to show a significant seaward motion, with displacements up to 5 cm along the coastline. As for the previous year, the displacement vectors on this side of the volcano generally increase from south to north, reaching a maximum of more than 8 cm along the Pernicana fault, but the pattern of the deformation is quite different from the previous comparison. In fact, the horizontal motion is much stronger on the northernmost part of the sliding flank; conversely, the lowermost stations show smaller displacements and an opposite vertical motion with respect to the previous year. In addition, the north-easternmost block shows an anomalous uplift (more than 8 cm) and a horizontal motion similar

Table 1. Displacements Measured From 2004 to 2005[a]

Station	Long.	Lat.	East	North	Up	Err. East	Err. North	Err. Up	Inverted
CAP	494784	4177300	0.028	−0.005	−0.032	0.001	0.001	0.003	X
CAS	523288	4191440	−0.002	0.001	0.034	0.002	0.002	0.007	
CES	474743	4188987	0.000	0.000	0.000	Fixed	Fixed	Fixed	
CIT	505242	4179808	0.007	−0.014	−0.016	0.001	0.001	0.005	X
CRI	508252	4183202	0.040	−0.022	−0.012	0.002	0.002	0.006	
CRP	480290	4164968	−0.010	0.003	−0.041	0.003	0.003	0.006	
EBAG	514170	4172804	0.041	−0.028	0.012	0.001	0.001	0.004	X
EDAM	500818	4185976	0.001	−0.020	0.018	0.001	0.001	0.004	X
EFAR	507276	4171590	0.004	−0.001	0.012	0.001	0.001	0.003	X
EMAL	493939	4182689	0.012	−0.015	0.009	0.001	0.001	0.003	X
EMEG	493585	4179668	0.024	−0.010	−0.016	0.001	0.001	0.003	X
EMFN	507942	4176492	0.007	−0.018	−0.004	0.001	0.001	0.004	X
EMGL	492816	4175439	0.024	0.004	−0.045	0.001	0.001	0.003	X
ENIC	501734	4162974	0.006	0.006	0.003	0.001	0.001	0.002	X
EPDN	501478	4179831	0.011	−0.016	−0.088	0.001	0.002	0.004	
ESPC	502417	4171701	0.007	0.011	−0.006	0.001	0.001	0.003	X
ESTP	505280	4172062	0.002	−0.003	0.021	0.001	0.001	0.004	X
ESVN	511199	4171089	0.012	−0.012	0.005	0.001	0.001	0.005	X
EW01	498296	4170453	0.009	0.016	−0.034	0.004	0.004	0.009	X
EW02	498592	4171824	0.003	0.023	−0.030	0.005	0.006	0.012	X
EW03	498134	4171672	0.004	0.031	−0.076	0.004	0.004	0.008	
EW04	498876	4172278	0.014	0.018	−0.043	0.005	0.006	0.011	X
EW05	500827	4172590	0.004	0.021	−0.061	0.006	0.006	0.014	X
EW06	501303	4172684	−0.001	0.037	−0.067	0.007	0.007	0.013	X
EW07	501908	4172296	0.021	−0.025	0.047	0.018	0.015	0.037	
EW08	502933	4172455	−0.019	0.012	−0.018	0.007	0.007	0.011	X
EW09	503520	4172506	−0.020	0.015	−0.019	0.006	0.006	0.010	X
EW10	501860	4171758	0.000	0.020	−0.046	0.008	0.007	0.015	X
EW11	502572	4171155	0.003	0.012	−0.008	0.006	0.006	0.013	X
EW12	502658	4170200	0.002	0.007	0.015	0.006	0.006	0.010	X
FOPE	506145	4167883	0.003	0.003	0.012	0.002	0.002	0.005	X
GIA	515723	4174501	0.054	−0.035	0.063	0.003	0.003	0.007	
GONA	517774	4181581	0.011	−0.007	0.030	0.002	0.002	0.006	X
INGV	507254	4151854	0.000	0.000	0.000	Fixed	Fixed	Fixed	X
ISLA	514706	4157124	0.032	−0.010	0.023	0.001	0.001	0.003	
L23	503092	4184205	0.008	−0.027	−0.034	0.002	0.002	0.005	X
LAM	501013	4185857	0.002	−0.019	−0.003	0.003	0.003	0.006	X
MANG	514920	4169690	0.028	−0.024	0.000	0.002	0.002	0.006	X
MDGR	515243	4160699	0.047	−0.009	−0.027	0.001	0.001	0.005	
MIL	509309	4176053	0.006	−0.038	0.002	0.001	0.001	0.006	X
MOSC	511928	4173822	0.013	−0.031	0.001	0.002	0.002	0.007	X
MPL	501671	4162063	0.005	−0.001	−0.011	0.002	0.002	0.004	X
MTSE	508704	4163780	0.016	0.002	−0.019	0.002	0.002	0.005	X
NS01	502153	4183269	0.014	−0.023	−0.047	0.004	0.004	0.008	
NS02	501283	4182458	0.019	−0.029	−0.052	0.004	0.004	0.007	
NS03	500860	4181959	0.016	−0.031	−0.071	0.004	0.004	0.008	
NS05	500575	4181049	0.021	−0.024	−0.114	0.004	0.004	0.007	
NS06	500462	4180451	0.018	−0.008	−0.122	0.004	0.004	0.008	
NS07	500609	4180037	0.014	−0.020	−0.116	0.004	0.004	0.010	
NS08	500188	4179785	0.035	−0.004	−0.109	0.005	0.005	0.012	
NS09	499284	4179619	0.031	−0.008	−0.085	0.004	0.005	0.010	
NS21	499579	4173308	0.008	0.030	−0.073	0.001	0.002	0.004	X
NUN	495831	4179544	0.029	−0.018	−0.034	0.001	0.001	0.004	X
OBS	501344	4180163	0.017	−0.006	−0.036	0.004	0.004	0.008	X
PDAP	512604	4165017	0.013	−0.019	0.014	0.002	0.002	0.005	X
PDG	488867	4177329	0.008	−0.006	−0.010	0.001	0.001	0.003	X
PER1	511618	4183057	0.038	−0.037	0.034	0.001	0.001	0.005	
PER2	511359	4183505	0.038	−0.024	0.017	0.003	0.003	0.006	
PER3	511780	4183595	0.012	−0.009	0.030	0.003	0.003	0.006	
PER4	511894	4183775	−0.005	−0.003	0.037	0.003	0.003	0.006	
PER5	511632	4183833	−0.005	−0.005	0.041	0.003	0.003	0.006	
PER6	511529	4183719	−0.004	−0.009	0.023	0.003	0.003	0.006	
PISA	509666	4168643	0.008	−0.003	0.014	0.002	0.002	0.006	X
PLU	499117	4179836	0.036	−0.010	−0.116	0.006	0.006	0.013	
ROC	500461	4200342	0.000	0.000	0.000	Fixed	Fixed	Fixed	
RPN1	509697	4184197	−0.001	−0.011	−0.003	0.003	0.003	0.006	
RPN2	509349	4184345	0.002	−0.009	−0.005	0.003	0.003	0.006	
RPN3	509211	4183626	0.042	−0.026	−0.014	0.003	0.003	0.006	
RPN4	509727	4183889	0.041	−0.027	0.002	0.003	0.003	0.006	
RPN5	509827	4183375	0.046	−0.022	−0.019	0.003	0.003	0.006	
SANT	515920	4178538	0.043	−0.030	0.012	0.003	0.003	0.006	X
SCOR	513800	4180818	0.060	−0.037	0.011	0.002	0.002	0.006	
SGBO	513674	4167958	0.020	−0.018	0.018	0.001	0.001	0.004	X

Table 1. (continued)

Station	Long.	Lat.	East	North	Up	Err. East	Err. North	Err. Up	Inverted
SGMB	514240	4176820	0.036	−0.041	0.038	0.002	0.002	0.007	X
SSBI	519327	4183763	0.008	0.006	0.029	0.003	0.003	0.007	
STAZ	517466	4167441	0.059	−0.023	0.016	0.001	0.001	0.005	
TARC	519072	4174522	0.046	−0.030	0.072	0.001	0.002	0.006	
TERR	513733	4185997	−0.002	0.001	0.024	0.001	0.001	0.006	
TMPR	502194	4184888	0.004	−0.023	0.008	0.002	0.002	0.005	X
TUR	490508	4174002	0.013	0.001	−0.031	0.001	0.001	0.004	X

[a]Units in meters. Coordinates are in UTM projection, zone 33N. 2-sigma errors are also reported. The "X" in the last column indicates that the motion of station was used in the inversion.

to that of the closer southern stations. Even this pattern results from the motion of only one station (GONA) lying in this block. It is unlikely to be due to measurement errors especially for the horizontal component, thanks to the self-centering benchmarks that avoid station setup errors; furthermore, each station is usually measured at least twice during a GPS survey. The motion of this station in this period could reasonably be due to the stronger displacements affecting the northernmost part of the sliding flank (along the Pernicana fault). Furthermore, while in 2004–2005 the displacements along the Pernicana fault show the same ESE azimuth of its easternmost segment, in 2005–2006 they show a more pronounced eastward component, toward the fault. In this frame, the motion of the northeastern flank causes a compression on the WNW-ESE branch of the fault, pushing the triangular block that behaves like a "flower structure", as already described by *Bonforte et al.* [2007a], and forcing it to move and uplift. Finally, the increase of the displacements toward the upper part of the eastern flank in 2005–2006 is imputable to the inflation of the volcano.

6. Data Inversion and Modeling

[16] The 2004–2005 GPS observations on Mt. Etna show a centripetal contraction of the western flank and an independent southeast movement of the eastern sector, requires a combination of two processes: a deflation due to the contracting magma body and sliding of the eastern flank.

[17] The 2004–2005 GPS observations on Mt. Etna, that show a centripetal contraction of the western flank and an independent southeast movement of the eastern sector, suggest a combination of two processes.

[18] Conversely, the ground deformation pattern of the 2005–2006 period shows a dilating phase where the volcano restarted to inflate, also accompanied by the southeastward motion of the eastern flank.

[19] For this reason, we have chosen to model each of these two periods with two different ground deformation sources: the first source was an *Okada* [1985] dislocation plane beneath the eastern flank common to both periods, and the second one was a *Davis* [1986] point-pressurized cavity of ellipsoidal shape, arbitrarily oriented in the half-space, to model the opposite deflation-inflation mechanism acting during the 2004–2005 and 2005–2006 periods respectively.

[20] We fixed the position and geometry of the dislocation plane to those found by *Bonaccorso et al.* [2006] who inverted GPS data from 2003–2004 time interval in order to make the resulting kinematics comparable to that affecting the volcano in the previous year.

[21] We inverted both GPS motion data sets (2004–2005 and 2005–2006) using an optimization algorithm implemented by *Nunnari et al.* [2005] based on the Genetic Algorithm (GA).

[22] GA is generally better suited than typical gradient-based techniques to find global minima for non-linear optimization problems with many variables. Starting with an initial range of models, the GA progressively modifies the solution by incorporating the evolutionary behavior of "biological" systems [e.g., *Tiampo et al.*, 2004]. The search process is stopped when d = 99% or when the maximum number of generation model (in our case 100000) is achieved. The goodness of each solution is measured by the index of agreement (*d)*

$$d = 1 - \frac{\sum_{i=l}^{N} (P_i - O_i)^2}{\sum_{i=l}^{N} \left(|P_i - \bar{O}| + |O_i - \bar{O}|\right)^2}$$

where N represents the number of measured points, O_i and P_i the observed and predicted values, respectively, and $\bar{O}$ their mean values [*Nunnari et al.*, 2005].

[23] We inverted our data sets, searching for both pressure and planar sources together in a homogeneous elastic half-space. In this way, the inversion process was able to search the global minimum by adjusting all parameters of both sources simultaneously.

6.1. The 2004–2005 Data Set

[24] A preliminary search was performed using the whole 3-D displacement data set, but the large residuals observed on the NE Rift zone and on many of the easternmost stations of the network suggested excluding these points from the inversion procedure because the local structural framework probably caused the observed anomalous deformation. Thus the inverted data set comprised 44 benchmarks. The search grid parameters and results of the GA search are summarized in Table 3. The solution converged to a final fitness value of 84%, and the final result is in agreement with the effect produced by a deflating source elongated horizontally and located SE of the summit craters at a depth of ~4.5 km below sea level (SX = 500701 m, SY = 4175402 m, in UTM reference frame; SZ = 4562 m b.s.l.), with the semi-major axis length, a, comparable to that of the b axis, and semi axis c about 1/10 that of a. The three Euler angles (indicating the ellipsoid orientation) show that the ellipsoid dips about 26° toward NW (see Figure 4a).

[25] The model sliding plane has normal and dextral components of movement of 2.7 and 2.5 cm respectively.

Table 2. Displacements Measured From 2005 to 2006[a]

Station	Long.	Lat.	East	North	Up	Err. East	Err. North	Err. Up	Inverted
CAP	494784	4177300	−0.027	−0.010	0.016	0.001	0.001	0.002	X
CIT	505242	4179808	0.066	−0.004	0.024	0.002	0.002	0.005	X
CRI	508252	4183203	0.072	−0.021	0.001	0.002	0.002	0.004	
CTNV	474654	4161001	−0.001	0.007	0.008	0.001	0.001	0.003	X
EARS	495519	4168537	−0.008	−0.030	0.005	0.001	0.001	0.003	X
EBAG	514170	4172804	0.030	−0.020	−0.009	0.001	0.001	0.001	X
ECES	475144	4188721	0.000	0.000	0.000	Fixed	Fixed	Fixed	
ECNL	499733	4169033	0.020	−0.039	−0.030	0.001	0.001	0.002	X
ECPN	498812	4177383	0.006	−0.010	0.025	0.001	0.001	0.001	X
EDAM	500818	4185976	0.005	0.023	0.011	0.001	0.001	0.001	X
EFAR	507276	4171590	0.021	−0.022	−0.001	0.001	0.001	0.001	X
ELEO	515207	4171699	0.037	−0.018	−0.014	0.001	0.001	0.002	X
EMAL	493939	4182689	−0.007	0.014	0.004	0.001	0.001	0.002	X
EMEG	493585	4179668	−0.021	0.003	0.012	0.001	0.001	0.001	X
EMFN	507942	4176492	0.043	−0.029	0.001	0.001	0.001	0.001	X
EMGL	492816	4175439	−0.027	−0.015	0.038	0.001	0.001	0.001	X
EMIR	495213	4173307	−0.028	−0.034	0.018	0.001	0.001	0.003	X
EMSL	498778	4167212	0.000	−0.027	0.008	0.001	0.001	0.004	X
ENIC	501734	4162974	0.005	−0.014	−0.002	0.001	0.001	0.001	X
EPDN	501478	4179831	0.029	0.022	0.037	0.001	0.001	0.001	X
EPEL	503358	4165274	0.009	−0.014	0.010	0.001	0.001	0.003	X
EPLU	498743	4179754	0.011	0.009	0.027	0.001	0.001	0.001	X
ESLN	497737	4171800	0.001	−0.036	0.015	0.001	0.001	0.002	X
ESPC	502417	4171701	0.013	−0.018	0.004	0.001	0.001	0.001	X
ESTP	505280	4172062	0.017	−0.014	−0.009	0.001	0.001	0.003	X
ESVN	511199	4171089	0.018	−0.025	0.000	0.001	0.001	0.004	X
ETAR	502729	4168544	0.010	−0.020	0.001	0.001	0.001	0.004	X
EVRS	491489	4170313	−0.015	−0.014	0.007	0.001	0.001	0.003	X
EW01	498296	4170453	0.010	−0.041	0.026	0.003	0.003	0.006	X
EW02	498592	4171824	0.011	−0.038	0.035	0.004	0.005	0.009	X
EW03	498134	4171672	0.004	−0.044	0.048	0.005	0.005	0.010	X
EW04	498876	4172278	0.000	−0.042	0.042	0.005	0.006	0.011	X
EW05	500827	4172590	0.012	−0.035	0.051	0.006	0.006	0.011	X
EW06	501303	4172684	0.011	−0.030	0.052	0.004	0.005	0.010	X
EW07	501908	4172296	0.019	−0.028	0.039	0.007	0.008	0.013	X
EW08	502933	4172455	0.019	−0.028	0.011	0.005	0.006	0.009	X
EW09	503520	4172506	0.038	−0.040	0.048	0.007	0.009	0.014	X
EW10	501860	4171758	0.011	−0.017	0.043	0.009	0.008	0.022	X
EW11	502572	4171155	0.030	−0.027	0.012	0.007	0.007	0.017	X
EW12	502658	4170200	0.030	−0.031	0.023	0.005	0.005	0.010	X
FOPE	506145	4167883	0.013	−0.021	−0.033	0.001	0.001	0.004	X
GIA	515723	4174501	0.036	−0.012	−0.037	0.002	0.002	0.007	X
GONA	517774	4181581	0.056	−0.031	0.084	0.001	0.001	0.006	
INGV	507254	4151854	0.000	0.000	0.000	Fixed	Fixed	Fixed	X
ISLA	514706	4157124	0.029	0.004	0.000	0.001	0.001	0.002	X
L23	503093	4184205	0.024	0.025	0.035	0.002	0.002	0.004	X
MANG	514920	4169690	0.032	−0.019	−0.017	0.002	0.002	0.005	X
MDGR	515243	4160699	0.041	−0.018	0.001	0.002	0.002	0.006	X
MIL	509310	4176053	0.043	−0.030	0.000	0.001	0.001	0.005	X
MONT	501231	4208427	0.000	0.000	0.000	Fixed	Fixed	Fixed	
MOSC	511928	4173822	0.030	−0.029	−0.016	0.001	0.001	0.005	X
MPL	501671	4162063	0.003	−0.013	−0.005	0.001	0.001	0.004	X
NS01	502153	4183269	0.022	0.022	0.035	0.004	0.004	0.008	X
NS02	501283	4182458	0.023	0.039	0.046	0.005	0.005	0.010	X
NS03	500860	4181959	0.025	0.040	0.055	0.004	0.005	0.010	X
NS05	500575	4181049	0.017	0.038	0.041	0.005	0.005	0.011	X
NS06	500462	4180451	0.016	0.036	0.070	0.006	0.006	0.012	X
NS07	500610	4180037	0.015	0.033	0.082	0.006	0.006	0.013	X
NS21	499579	4173308	0.014	−0.037	0.032	0.002	0.002	0.004	X
NUN	495831	4179544	−0.018	0.013	0.037	0.001	0.001	0.004	X
OBS	501344	4180163	0.027	0.030	0.080	0.003	0.003	0.005	X
PDAP	512604	4165017	0.021	−0.019	−0.001	0.001	0.001	0.004	X
PDG	488867	4177329	−0.019	−0.005	0.018	0.001	0.001	0.002	X
PER1	511618	4183057	0.075	−0.032	−0.025	0.002	0.002	0.004	
PER2	511359	4183505	0.074	−0.032	−0.008	0.003	0.003	0.004	
PER3	511780	4183595	0.035	0.002	0.003	0.003	0.003	0.005	
PER4	511894	4183775	0.009	0.003	0.008	0.003	0.003	0.005	
PER5	511632	4183833	0.009	0.003	−0.019	0.003	0.003	0.005	
PER6	511529	4183719	0.007	0.007	0.007	0.003	0.003	0.005	
PISA	509666	4168643	0.023	−0.020	−0.010	0.002	0.002	0.006	X
RPN1	509697	4184197	0.000	0.006	0.017	0.003	0.003	0.006	
RPN2	509349	4184345	0.001	0.012	0.007	0.003	0.003	0.005	
RPN3	509211	4183626	0.083	−0.019	0.013	0.003	0.003	0.006	

Table 2. (continued)

Station	Long.	Lat.	East	North	Up	Err. East	Err. North	Err. Up	Inverted
RPN4	509727	4183889	0.084	−0.018	−0.007	0.003	0.003	0.006	
RPN5	509828	4183375	0.080	−0.022	0.024	0.003	0.003	0.005	
SANT	515920	4178538	0.040	−0.022	−0.026	0.002	0.002	0.006	X
SCOR	513800	4180818	0.072	−0.035	0.001	0.001	0.001	0.004	X
SGBO	513675	4167958	0.022	−0.016	0.011	0.001	0.001	0.002	X
SGMB	514240	4176820	0.035	−0.023	−0.021	0.001	0.002	0.006	X
SSBI	519327	4183763	0.003	0.003	0.004	0.003	0.003	0.006	
STAZ	517466	4167441	0.039	−0.018	−0.027	0.001	0.001	0.005	X
TARC	519072	4174522	0.04	−0.006	−0.085	0.001	0.001	0.005	
TERR	513733	4185997	0.007	0.005	−0.001	0.001	0.001	0.004	X
TMPR	502194	4184888	0.015	0.024	0.025	0.001	0.001	0.003	X
TUR	490508	4174002	−0.019	−0.006	0.004	0.001	0.001	0.002	X

[a]Units in meters. Coordinates are in UTM projection, zone 33N. 2-sigma errors are also reported. The "X" in the last column indicates that the motion of station was used in the inversion.

[26] The ground motions observed at the easternmost stations of the network between 2004 and 2005 are greater than these predicted by the model, revealing an underestimation of the sliding by the model. This misfit is due to the superimposition of the radial pattern produced by the contraction to the spreading dynamics that act in opposite ways on this side of the volcano. Furthermore, the ground deformation pattern on the eastern flank during the 2003–2004 deflation is markedly inhomogeneous and cannot be perfectly modeled by a unique source such as a wide sliding plane beneath the entire flank.

6.2. The 2005–2006 Data Set

[27] For this second inversion process, we have used the whole 3-D displacement data set, and we obtained a good fitness value of 92%. We didn't need to exclude any benchmarks because of the more uniform ground deformation pattern.

[28] The model source parameters define an ellipsoid elongated source located beneath the summit craters at a depth of ~3.5 km below sea level (SX = 499096 m, SY = 4177864 m, in UTM reference frame; SZ = 3692 m b.s.l.), with the semi-mayor axis of length, a, almost four times those of b and c. The three Euler angles indicate a near-vertical prolate ellipsoid.

[29] The sliding plane motion components results are in agreement with a dislocation plane with a main normal (4.6 cm) and minor dextral component (2.5 cm).

[30] The fit for both inversion processes is very good and we have a reduced chi-square value of 1.040 and 1.005 cm, with an average misfit of the horizontal and vertical components always less than 0.7 cm and 1.5 cm respectively, in good agreement with typical GPS precision.

[31] The comparison between the observed and the expected displacement vectors are reported in Figure 4b. The better fit of the 2005–2006 period is evident, especially

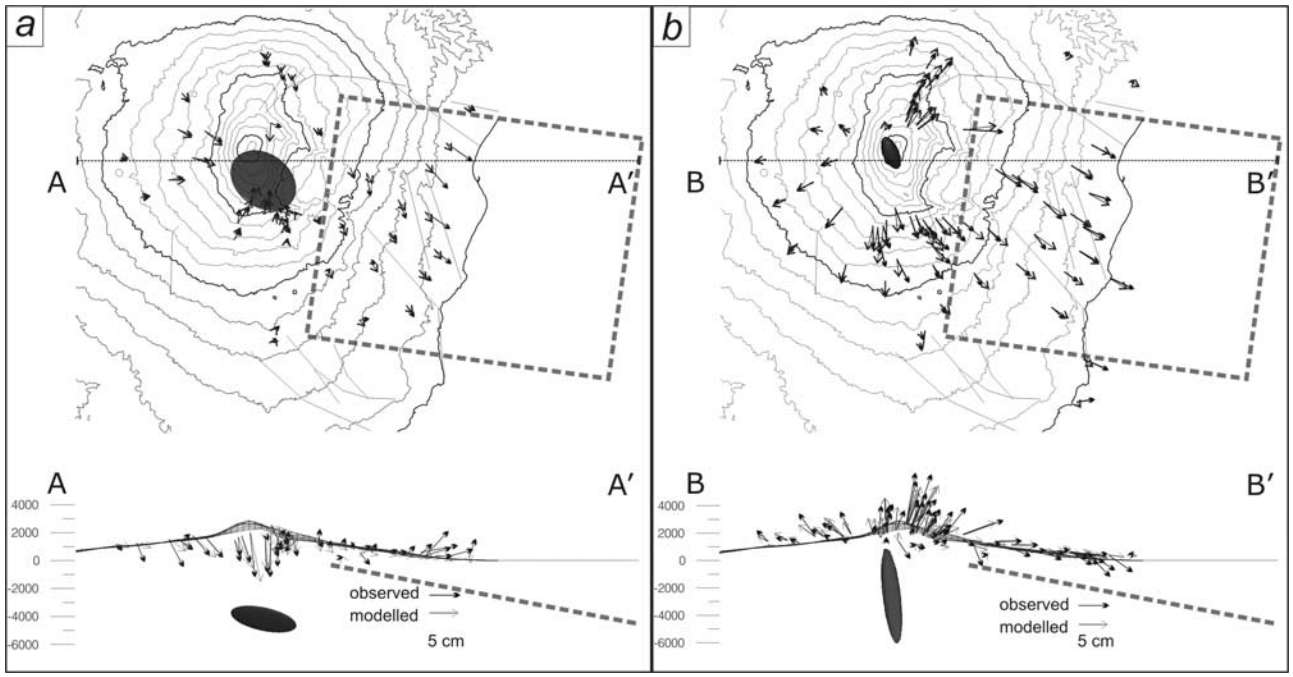

Figure 4. Comparison between observed (black arrows) and expected (gray arrows) horizontal displacements relevant to each time interval: (a) July 2004–July 2005; (b) July 2005–June 2006; A-A-A′ and B-B′ E–W sections of the volcano. Modeled sources are also reported.

Table 3. Results, Ranges and Fitness Parameters of the GA Optimization Search for the 2004–2005 and 2005–2006 Ground Deformation Data Inversions

Searched Parameters	Returned Value (44 points) 2004–2005	Returned Value (71 points) 2005–2006	Minimum	Maximum
	OKADA			
Dip	11.15	11.15	*Fixed to Bonaccorso et al.* [2006]	
Azimuth	8	8	*Fixed to Bonaccorso et al.* [2006]	
Length, m	20269	20269	*Fixed to Bonaccorso et al.* [2006]	
Width, m	25000	25000	*Fixed to Bonaccorso et al.* [2006]	
Strike, m	−0.0274	−0.0249	−0.5	0
Dip, m	−0.0255	−0.0461	−0.5	0.5
Opening, m	0	0	*Fixed to Bonaccorso et al.* [2006]	
Depth, m	1612	1612	*Fixed to Bonaccorso et al.* [2006]	
Latitude, m	505375	505375	*Fixed to Bonaccorso et al.* [2006]	
Longitude, m	4172644	4172644	*Fixed to Bonaccorso et al.* [2006]	
	DAVIS			
ΔP*Volume/μ(mc)	$-2.27*10^6$	$1.39*10^7$	$-3*10^{11}$	$3*10^{11}$
1^ Euler angle (*Vert to c-axis*)	154	−94.68	−180	180
2^ Euler angle (*North to a-axis*)	68.56	−36.67	−180	180
3^ Euler angle (rotation *a on perp c-axis*)	−15	107.17	−180	180
b/a	0.837	0.20	0.1	0.99
c/a	0.1	0.16	0.1	0.68
X*s*-(*m*)	500701	499096	498000	501000
Y*s*-(*m*)	4175402	4177864	4170000	4185000
Depth (*m*)	−5562	−4692	−8000	−1000
	Fitness parameters			
Fitness	16.28	7.91		
Horizontal average misfit, m	0.00732	0.00595		
Vertical average misfit, m	0.01429	0.010752		
Standard deviation east, m	0.0101	0.0085		
Standard deviation north, m	0.0100	0.00658		
Standard deviation vert, m	0.0162	0.01381		
X^2	1.050388	0.996366		
a-post. Tot. dev.st to reduced X^2 = 1, m	0.01040	0.010056		

in the eastern part of the network where the inhomogeneous pattern during 2004–2005 prevents a simple modeling with a unique dislocation source in a homogeneous elastic half-space.

7. Discussion

[32] During the 2004–2006 interval, two main features of the ground deformation pattern of Mt. Etna have been detected: a deflation-inflation cycle between two (2004–2005 and 2006) eruptions, in both cases accompanied by a seaward motion of the eastern flank.

[33] During the 2004–2005 eruption, a degassed magma was emitted, that was already residing inside the volcano after previous eruptions, and that intruded passively due to the exceptional extension on the summit area caused by the high sliding rate of the eastern flank of the volcano (almost 9 cm of slip on the modeled source from 2003 to 2004) [*Bonaccorso et al.*, 2006]. The wide contraction measured during the eruption (Figure 3a) testifies how the emptying of this shallow magma storage also caused a drainage of a

Table 4. Ground Deformation Sources at Mt. Etna Since 1992 From Literature

ID	Time Interval	Source Type	Behavior of the Source	Horizontal Position Lat.	Horizontal Position Long.	Depth, km b.s.l.	Data	Reference
1	May 1992 – Nov 1993	Davis type	depressurization	478.62	499.21	3.1 b.s.l.	EDM, GPS, Tilt	*Bonaccorso* [1996]
2	Sept 1993 – Jul 1994	Mogi type	pressurization	4179.00	500.00	3.8 b.s.l.	GPS	*Puglisi et al.* [2001]
3	Jun 1993 – Oct 1995	Yang type	pressurization	4177.67	499.89	4.8 b.s.l.	InSAR	*Lundgren et al.* [2003]
4	Jul 1996 – Jul 1997	Mogi type	pressurization	4180.90	497.61	9.3 b.s.l.	GPS	*Puglisi and Bonforte* [2004]
5	Sept 1993 – Jul 1997	Mogi type	pressurization	4179.45	496.96	6.8 b.s.l.	GPS	*Palano et al.* [2007]
6	Sept 1993 – Jul 1997	Davis type	pressurization	4177.94	500.70	4.0 b.s.l.	EDM, GPS	*Bonaccorso et al.* [2005]
7	Sept 1993 – Jul 2000	Mogi type	pressurization	4181.37	496.93	8.1 b.s.l.	GPS	*Palano et al.* [2007]
8	Jul 1994 – Jul 2001	Mogi type	pressurization	4180.50	499.00	6.2 b.s.l.	GPS	*Houlié et al.* [2006]
9	Jul 2003 – Jul 2004	Mogi type	pressurization	4177.48	499.63	2.9 b.s.l.	GPS	*Bonaccorso et al.* [2006]

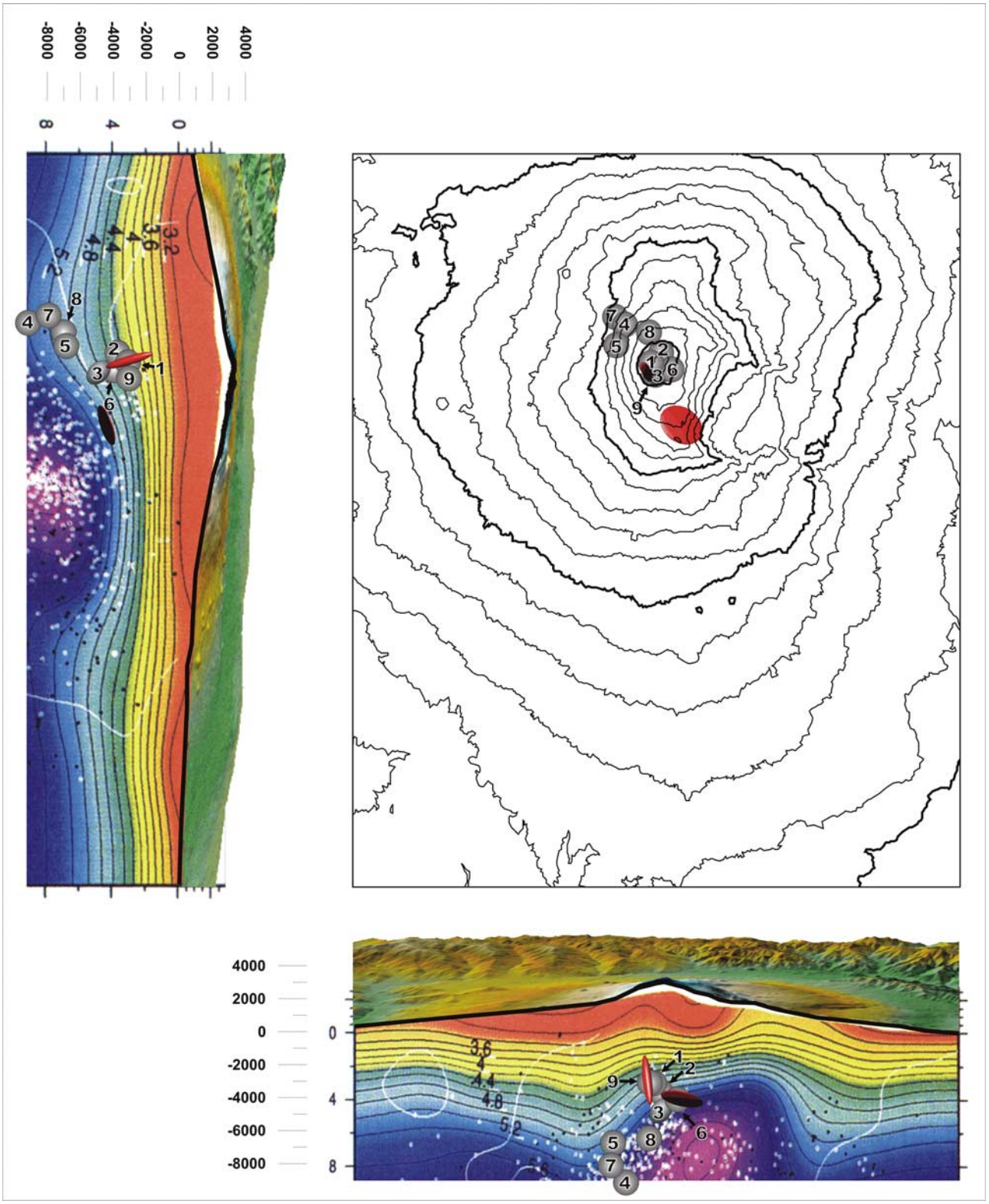

Figure 5. Schematic map and cross sections (N–S and E–W) showing the geometrical relationships between the ground deformation sources modeled in this work and those proposed by several authors since 1992 (see Table 4 for details). Source dimensions are not in scale.

deeper magma reservoir that data inversions define as a sill-shaped source (Figure 4a and Table 3) located at a depth of about 4.5 km b.s.l. beneath the upper south-eastern flank of the volcano. The depressurizing source is located in the zone where both the inflating source detected by *Bonaccorso et al.* [2005] during the 1993–1997 inflation period and the point pressure source active before the 2004–2005 eruption [*Bonaccorso et al.*, 2006] were already located by previous modeling of GPS data (Figure 5 and Table 4). Also the modeling of the deflation phase which accompanied the long 1992–1993 eruption showed a depressurizing source located in that position [*Bonaccorso*, 1996]. All the pressure sources active during the last decade (Table 4) are located at the NW top of the high density body (Figure 5) detected from seismic tomography by *Chiarabba et al.* [2000]. The distribution of the ground deformation sources modeled over time since 1993, would confirm that the magma prevalently rises along the north-western border of a body with high seismic velocities (Vp) and that the upper part of the high Vp body is a region of magma storage as inferred by *Patanè et al.* [2003]. In addition, the ground deformation sources clearly define a volume of intermediate storage (5 ± 2 km b.s.l.) which characterized the feeding system of the volcano during the last decade, as shown in Figure 5 and Table 4. In this context, the diking of 2001 and 2002–2003 lateral eruptions were consistent with an over-pressuring in this intermediate storage source, which fractured its upper limit at about 3 km b.s.l and caused the magma intrusion along eccentric dikes, provoking violent explosive-effusive eruptions. The eccentric dike intrusions accompanying these two eruptions induced an exceptional stress on the Mt. Etna edifice, inducing an acceleration of the sliding of the unstable eastern side of the volcano. From the 2002–2003 eruption on, in fact, the sliding of the eastern flank showed an exceptionally high velocity that continued during the years following the eruption even with a minor slip rate. In fact, the total slip calculated on the same Okada model, decreased from almost 9 cm during 2003–2004 [*Bonaccorso et al.*, 2006] to 5 cm in 2005–2006. The upper part of the volcano edifice underwent the maximum tension that favored the opening of tensile fracture from which the resident magma poured out passively in the 2004–2005 eruption [*Bonaccorso et al.*, 2006]. This mechanism was new and unusual for the volcano but the deflation accompanying the 2004–2005 eruption confirms a depressurizing source (Figure 4a) located in a similar zone to the previous modeled sources (Figure 5). Therefore we can conclude that also for the 2004 eruption, even if the final fracturing mechanism was different from the classic previous intrusions, the intermediate storage maintained its previous position.

[34] It is interesting to note that the areal dilatation accumulated by the entire GPS network (see Figure 2a), after a very long inflation period since 1992, has never returned to the initial value, showing an ever increasing trend, with strong accelerations during the 2001 and 2002–2003 eruptions. This contrasts with the contractions measured during the same periods, calculated over a triangle formed by three stations lying on the northern (EDAM) western (PDG) and south-southwestern (ESLN) flanks, on the stable part of the volcano (that is not affected by sliding dynamics). This is mainly due to the effect of the sliding eastern flank of the volcano that produces a continuing dilatation of this part of the network. However, even considering only the stable part of the volcano, the contraction episodes do not entirely recover the dilatation accumulated since 1992. During the eruptive phase that started in 1999, the areal dilatation on the stable part continues to show a slightly ascending trend overall (with a much lower rate with respect to the entire network), because the contraction periods do not recover even the immediately preceding short term dilatation. This would imply that a fraction of the new magma pressurizing the plumbing system during the long recharging phase from 1992 to 1999 and, with a lower rate, from 2001 to 2006, was permanently stored, probably solidifying along the western border of the high Vp body, as suggested by *Laigle et al.* [2000]. Consequently, during the depressurizations of the magmatic sources, the volcano only partially recovers the deformation accumulated beforehand.

[35] The different trends between the cumulative areal dilatation on the total network and on the stable triangle since 2001, confirms the decoupling of the eastern flank from the rest of the volcano. The apparently slower sliding dynamics during the 2004–2005 deflation, reveals the disarrangement of the eastern side of the volcano into different moving blocks with different behaviors, as already evidenced in *Bonforte and Puglisi* [2006], controlled by complex local fault systems.

[36] After the end of the 2004–2005 eruption, the volcano started to re-inflate and a vertically elongated pressurizing source was located by GPS data inversion at a depth of about 3 km b.s.l. The center of the inflation source (Figure 4b and Table 3) shifted slightly north-westward (beneath the summit craters) and is rather shallower than the previous ones. The pressurizing source modeled for the 2005–2006 time interval indicates a re-filling of the shallower plumbing system of the volcano by magma rising up from depth. In fact, the ellipsoidal pressurization source is vertically elongated, well reproducing a vertical path from the western side of the high Vp body toward the summit craters. This could indicate a change in the geometry of the feeding system after the 2004–2005 eruption, with a new and shallower magma storage that reasonably allowed the resumption of volcanic activity at summit craters in 2006.

8. Conclusions

[37] In this work the ground deformation of Mt. Etna from 2004 to 2006 was analyzed. This period was accompanied by the September 2004 to March 2005 eruption and by a re-charging phase leading to an eruption starting in June 2006. During this period, an entire deflation-inflation cycle was detected, and the models obtained by inverting ground deformation data confirm and improve the imaging of the feeding system of the volcano.

[38] All the pressuring/depressuring storage sources modeled for the previous eruptions are positioned along the western side of the high Vp body revealed by seismic tomography. In this study the deflation source indicates the depletion of a horizontal sill-shaped source, located in the upper part of this body. Instead, the inflation reveals a refilling of the shallower vertical plumbing system of Mt.

Etna, reasonably related with the resumption of volcanic activity at the summit craters in 2006.

[39] The general trend of the areal dilatation of the GPS network since 1990, indicates that the spreading induced by the pressurizing of the plumbing system is mainly accumulated in a non-elastic behavior. The eastern flank is affected by a continuous eastward sliding, which became more marked after the NE intrusion of the 2002–2003 eruption. However, the more stable western sector also shows that the deformation accumulated during the long-lasting inflation phase from 1992 to 2001 was not recovered during the following eruptive phases, indicating a permanent deformation of the volcano and, consequently a permanent storage of non-erupted magma in the plumbing system.

[40] **Acknowledgments.** Authors are grateful to B. Puglisi, M. Cantarero, F. Calvagna, O. and S. Consoli, G. Brischetti, and R. Caruso that allowed the GPS surveys to be carried out. We thank M. Mattia and all the permanent GPS task force of INGV, section of Catania, for providing the data of the permanent network. Thanks are also due to S. Conway for his helpful revision of the English language and to G. Wadge and P. Lundgren for their critical review that helped us to profoundly improve the manuscript.

References

Allard, P., B. Behncke, S. D'Amico, M. Neri, and S. Gambino (2006), Mount Etna 1993–2005: Anatomy of an evolving eruptive cycle, *Earth Sci. Rev.*, *78*, 85–114, doi:10.1016/j.earscirev.2006.04.002.

Bonaccorso, A. (1996), Dynamic inversion of ground deformation data for modelling volcanic sources (Etna 1991–93), *Geophys. Res. Lett.*, *23*(5), 451–454.

Bonaccorso, A., S. Cianetti, C. Giunchi, E. Trasatti, M. Bonafede, and E. Boschi (2005), Analytical and 3-D numerical modelling of Mt. Etna (Italy) volcano inflation, *Geophys. J. Int.*, *163*, 852–862, doi:10.1111/j.1365-246X.2005.02777.x.

Bonaccorso, A., A. Bonforte, F. Guglielmino, M. Palano, and G. Puglisi (2006), Composite ground deformation pattern forerunning the 2004–2005 Mount Etna eruption, *J. Geophys. Res.*, *111*, B12207, doi:10.1029/2005JB004206.

Bonforte, A., and G. Puglisi (2003), Magma uprising and flank dynamics on Mount Etna volcano studied using GPS data (1994–1995), *J. Geophys. Res.*, *108*(B3), 2153, doi:10.1029/2002JB001845.

Bonforte, A., and G. Puglisi (2006), Dynamics of the eastern flank of Mt. Etna volcano (Italy) investigated by a dense GPS network, *J. Volcanol. Geotherm. Res.*, *153*(3–4), 357–369, doi:10.1016/jvolgeores.2005.12.005.

Bonforte, A., F. Guglielmino, M. Palano, and G. Puglisi (2004), A syn-eruptive ground deformation episode measured by GPS, during the 2001 eruption on the upper southern flank of Mt Etna, *Bull. Volcanol.*, *66*(4), 341–366.

Bonforte, A., S. Branca, and M. Palano (2007a), Geometric and kinematic variations along the active Pernicana fault: Implication for the dynamics of Mount Etna NE flank (Italy), *J. Volcanol. Geotherm. Res.*, *160*, 210–222, doi:10.1016/j.jvolgeores.2006.08.009.

Bonforte, A., D. Carbone, F. Greco, and M. Palano (2007b), Intrusive mechanism of the 2002 NE-rift eruption at Mt. Etna (Italy) modelled using GPS and gravity data, *Geophys. J. Int.*, *169*, doi:10.1111/j.1365-246X.2006.03249.x.

Borgia, A., L. Ferrari, and G. Pasquarè (1992), Importance of gravitational spreading in the tectonic and volcanic evolution of Mount Etna, *Nature*, *357*, 231–235.

Borgia, A., R. Lanari, E. Sansosti, M. Tesauro, P. Berardino, G. Fornaro, M. Neri, and J. B. Murray (2000), Actively growing anticlines beneath Catania from the distal motion of Mount Etna's decollement measured by SAR interferometry and GPS, *Geophys. Res. Lett.*, *27*(20), 3409–3412.

Bousquet, J. C., and G. Lanzafame (2004). The tectonics and geodynamics of Mt. Etna: Synthesis and interpretation of geological and geophysical data, in *Etna Volcano Laboratory*, *Geophys. Monogr. Ser.*, vol. 143, edited by A. Bonaccorso, S. Calvari, M. Coltelli, C. Del Negro, and S. Falsaperla, pp. 29–47, AGU, Washington, D.C.

Burton, M. R., et al. (2005), Etna 2004–2005: An archetype for geodynamically-controlled effusive eruptions, *Geophys. Res. Lett.*, *32*, L09303, doi:10.1029/2005GL022527.

Chiarabba, C., A. Amato, E. Boschi, and F. Barberi (2000), Recent seismicity and tomographic modeling of the Mount Etna plumbing system, *J. Geophys. Res.*, *105*(B5), 10923–10938.

Davis, P. M. (1986), Surface deformation due to inflation of an arbitrarily oriented triaxial elipsoidal cavity in an elastic half-space, with reference to Kilauea volcano, Hawaii, *J. Geophys. Res.*, *91*(B7), 7429–7438.

Froger, J.-L., O. Merle, and P. Briole (2001), Active spreading and regional extension at Mount Etna imaged by SAR interferometry, *Earth Planet. Sci. Lett.*, *187*, 245–258.

Houlié, N., P. Briole, A. Bonforte, and G. Puglisi (2006), Large scale ground deformation of Etna observed by GPS between 1994 and 2001, *Geophys. Res. Lett.*, *33*, L02309, doi:10.1029/2005GL024414.

Laigle, M., A. Hirn, M. Sapin, J. C. Lépine, J. Diaz, J. Gallart, and R. Nicolich (2000), Mount Etna dense array local earthquake P and S tomography and implications for volcanic plumbing, *J. Geophys. Res.*, *105*(B9), 21633–21646.

Livieratos, E. (1980), Crustal strains using geodetic methods, *Quaterniones Geodaesiae*, *3*, 191–211.

Lo Giudice, E., and R. Rasà (1992), Very shallow earthquakes and brittle deformations in active volcanic areas: The Etnean region as an example, *Tectonophysics*, *202*, 257–268.

Lundgren, P., P. Berardino, M. Coltelli, G. Fornaro, R. Lanari, G. Puglisi, E. Sansosti, and M. Tesauro (2003), Coupled Megma chamber and sector collapse slip observed with synthetic aperture radar interferometry on Mt. Etna volcano, *J. Geophys. Res.*, *108*(B5), 2247, doi:10.1029/2001JB000657.

Lundgren, P., F. Casu, M. Manzo, A. Pepe, P. Berardino, E. Sansosti, and R. Lanari (2004), Gravity and magma induced spreading of Mount Etna volcano revealed by satellite radar interferometry, *Geophys. Res. Lett.*, *31*, L04062, doi:10.1029/2003GL018736.

Nunnari, G., G. Puglisi, and F. Guglielmino (2005), Inversion of SAR data in active volcanic areas by optimization techniques, *Nonlin. Proc. Geophys.*, *12*, 863–870.

Okada, Y. (1985), Surface deformation due to shear and tensile fault in half-space, *Bull. Seismol. Soc. Am.*, *75*, 1135–1154.

Palano, M., G. Puglisi, and S. Gresta (2007), Ground deformation at Mt. Etna: A joint interpretation of GPS and InSAR data from 1993 to 2000. *Boll. Geofis. Teor. Appl.*, *48*(2), 81–98.

Patanè, D., P. De Gori, C. Chiarabba, and A. Bonaccorso (2003), Magma ascent and the pressurization of Mount Etna's volcanic system, *Science*, *299*, 2061–2063.

Puglisi, G., and A. Bonforte (2004), Dynamics of Mount Etna volcano inferred from static and kinematic GPS measurements, *J. Geophys. Res.*, *109*, B11404, doi:10.1029/2003JB002878.

Puglisi, G., A. Bonforte, and S. R. Maugeri (2001), Ground deformation patterns on Mt. Etna, between 1992 and 1994, inferred from GPS data, *Bull. Volcanol.*, *62*, 371–384.

Puglisi, G., P. Briole, and A. Bonforte (2004), Twelve years of ground deformation studies on Mt. Etna volcano based on GPS surveys, in *Etna Volcano Laboratory*, *Geophys. Monogr. Ser.*, vol. 143, edited by A. Bonaccorso, S. Calvari, M. Coltelli, C. Del Negro, and S. Falsaperla, pp. 321–341, AGU, Washington, D.C.

Rasà, R., R. Azzaro, and O. Leonardi (1996), Aseismic creep on faults and flank instability at Mt. Etna volcano, in *Volcano Instability on the Earth and Other Planets*, edited by W. M. McGuire, A. P. Jones, and J. Neuberg, *Geol. Soc. Lon.-Spec. Publ.*, *110*, 179–192, doi:10.1144/GSL.SP.1996.110.01.14, Geological Society of London, London.

Rust, D., and M. Neri (1996). The boundaries of large-scale collapse on the flanks of Mount Etna, Sicily, in *Volcano Instability on the Earth and Other Planets*, edited by W. M. McGuire, A. P. Jones, and J. Neuberg, *Geol. Soc. Lon.-Spec. Publ.*, *110*, 193–208, doi:10.1144/GSL.SP.1996.110.01.15, Geological Society of London, London.

Rust, D., B. Behncke, M. Neri, and A. Ciocanel (2005), Nested zones of instability in the Mount Etna volcanic edifice, Sicily, *J. Volcanol. Geotherm.*, *144*, 137–153, doi:10.1016/j.jvolgeores.2004.11.021.

Tiampo, K. F., J. Fernandez, G. Gentzsch, M. Charco, and J. B. Rundle (2004), Inverting for the parameters of a volcanic source using a genetic algorithm and a model for magmatic intrusion in elastic-gravitational layered Earth models, *Comput. Geosci.*, *30*(9–10), 985–1001, doi:10.1016/j.cageo.2004.07.005.

Walter, T. R., V. Acocella, M. Neri, and F. Amelung (2005), Feedback processes between magmatic events and flank movement at Mount Etna (Italy) during the 2002–2003 eruption, *J. Geophys. Res.*, *110*, B10205, doi:10.1029/2005JB003688.

A. Bonaccorso, A. Bonforte, F. Guglielmino, M. Palano, and G. Puglisi, Istituto Nazionale di Geofisica e Vulcanologia, Sezione di Catania–Piazza Roma, 2–95123, Catania, Italy. (bonforte@ct.ingv.it)